Current Topics in Electrochemistry
Vol. 23, 2021

Original Article

A novel theory on the mechanisms of generation, transport and release of oxygen gas and electronic current in anodic alumina film during Al anodizing

G. Patermarakis*

Department of Biomedical Engineering, School of Engineering, University of West Attica, Egaleo Park Campus, Agiou Spiridonos 17, Egaleo, Attiki, 12243, Greece.

ABSTRACT

The generation, transfer and release of oxygen and electronic current during galvanostatic growth of porous anodic alumina films (PAAFs) was studied and novel mechanisms were formulated. Oxygen release is visually detected above a first boundary of current density. Above it, oxygen release starts earlier and is enhanced with increasing current density but remains mildly detectable up to a much higher second boundary. Below but near it, the normal PAAF growth is transformed to abnormal, which is associated with emergence of local burning. Above it intense and massive oxygen release and electropolishing occur rapidly and successively. The high field in the barrier layer of the order 10^9 V m^{-1} polarizes the oxide lattice making it more open thereby enabling ionic migrations. It also polarizes the O^{2-} ions so that their electronic structure is destabilized. Field-activated processes generating electrons $O^{2-} \leftrightarrows O^{-1} + e^-$ and $O^{-1} \leftrightarrows O + e^-$ with overall $O^{2-} \leftrightarrows O + 2e^-$ are established and propagated, the first and third being thermochemically prone. Adjacent O atoms form O_2 and partly O_3, in the form of separate molecules and of nano-bubbles. Molecules and nano-bubbles formed in the oxide|electrolyte interface enter the pore filling solution directly and those formed in the barrier layer are released in this solution as the barrier layer is renewed and the pore walls are chemically dissolved. Then, molecules and nano-bubbles are transferred outwards. Laplace, van der Waals and Henry's law equations predict compressed nano-bubbles in equilibrium with high-concentration dissolved-oxygen. While remoting from pore bases, nano-bubbles shrink until their depletion. Local accumulation of nano-bubbles in the attached layer at spatial density above a critical one triggers their avalanche-like merge. Their merger is accompanied with pressure fall and volume expansion to larger nano-, micro- and macro-bubbles. The formulated mechanisms explain the results in this work and in the literature on the evolution of electronic current and oxygen and on the growth of peculiar PAAF nanostructures. Development of nano-porous anodes to optimize evolution of nano-bubbles/dissolved oxygen system is also discussed.

KEYWORDS: Al anodizing, porous alumina film, oxygen/electronic current, generation-transfer-release, mechanisms.

1. INTRODUCTION

Al anodization in suitable pore forming electrolytes, e.g. oxalic, sulphuric, phosphoric, tartaric, etc. acid, produces porous anodic alumina films (PAAFs) [1]. PAAFs grow in three sequential stages, the first and second transient short stages and the third steady-state stage where their structures become close-packed array of about hexagonal columnar cells [2-5]. Each cell contains

*Email id: gpaterm@uniwa.gr

an elongated pore vertical to Al surface, extending from top surface to near metal|oxide (m|o) interface, while a thin spherical sector shell-shaped barrier-type layer with thickness ≈ 1 nm per V of applied voltage exists among interface and pore bottom [2-5]. Some structural details of PAAF formed in H_2SO_4 [6], important for this work, appear in Figure 1.

The specific electrochemical behavior of Al anode and self-organized nano-structure of PAAF have made Al anodizing an exciting model process in solid-state electrochemistry [3, 4, 7, 8]. PAAFs are a fundamental tool to develop functional nanomaterials. Their specific properties such as structural, mechanical, physicochemical etc. find numerous applications in conventional engineering [8], modern science and nanoscience [7, 9-15] and currently developing technologies [16-22].

During PAAF growth, electrochemical processes occur in the barrier layer [5, 23, 24] (Figure 1). It consists of an inner almost pure oxide sub-layer towards the Al side and an outer one contaminated by small amounts of electrolyte anions and H^+. This composition distribution is imprinted across pore walls. Oxide is an amorphous/nanocrystalline material [3, 4, 25]. Despite the presence of contaminating ions, the main migrating ions in barrier layer are Al^{3+} and O^{2-} carrying almost the entire ionic current.

While this is a generally accepted model for ion migrations in the barrier layer of PAAF, various models have been proposed for the mechanism of pore nucleation and development. Mainly in the past decades it was widely adopted that the initial pore nucleation comes from a field-assisted local chemical dissolution of barrier layer surface and pore growth comes from redistribution of current and a field-assisted H^+ ion attack on the pore bottom [24, 26-30]. Newer models based on recrystallization of oxide formed in barrier layer and its densification towards the oxide surface [31-34], plastic flow [35-37] and development of

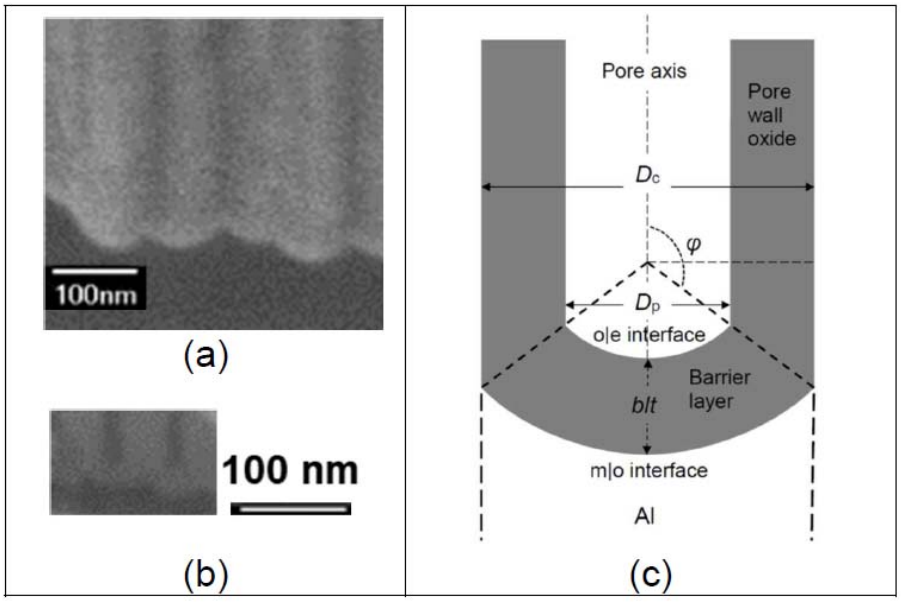

Figure 1. (a, b) Field emission scanning electron microscopy micrographs of the cross-sectional fractures of PAAFs formed in 0.51 M H_2SO_4 electrolyte at anodic potential (vs. SHE) 23.615 V, temperature 298 K and anodizing times 2430 s (a) and 2280 s (b) where the current density is 212.9 mA cm^{-2} and 43.3 mA cm^{-2}, respectively, [6]. (a) External geometry of the columnar cells detached *via* intercellular boundaries and of the corresponding barrier layer units in a region near Al substrate. (b) Cross section of spherical-sector shell-shaped barrier layer units. (c) Schematic cross section of a cell/pore unit of PAAF around the pore base region where the pore, pore wall, barrier layer and its thickness, *blt*, angle of pore axis with the boundary of pore wall and barrier layer, φ, the cell width, D_c, and pore base diameter, D_p, are shown.

stresses [38, 39] in barrier layer have also been reported.

A recent model [40, 41], using analytical mathematical equations, described the movements and trajectories of Al^{3+} and O^{2-}, embodied electrolyte anions and tracer species either in metal or pre-existing oxide. Their description in barrier layer region explains the growth of porous structure. This model invokes field-assisted dissolution, while stresses and plastic flow under stresses seem redundant. But, field-assisted dissolution actually means the ability of a solution to solvate the Al^{3+} ions ejected either electrochemically at pore bases or from chemical dissolution of pore walls [5, 31].

Extensive discussion has been made, mainly in the two last decades, on electronic current passing through barrier layer during PAAF growth [42-47]. It is related with evolution of oxygen gas and thus with reduced ionic current and oxide growth efficiency. Oxygen evolution was linked with the formation of pores, appearance of nano-cavities in barrier-type films and in the barrier layer and pore walls of PAAF and with modulated pores obtained by two- or three-step anodizing, where each step is performed in a different electrolyte solution [42-47]. Also, serrated porous structures, obtained in certain electrolytes and anodizing conditions, were generally ascribed to oxygen evolution together with plastic deformation [44, 48-50]. Recently the serrated/dendritic porous structure was associated with incessant termination/ generation of pores [51]. Electronic current was also associated with galvanoluminescence [52].

The release of oxygen in Al anode is clearly visible for various electrolytes and anodizing conditions [23, 43, 45]. During e.g. galvanostatic anodizing, for each electrolyte its release rate seems to rise with increasing current density (j) and decreasing temperature. Also, at given conditions it is generally higher for certain electrolytes. But it has been proved repetitively that the consumed Al almost precisely obeys Faraday's law [23, 31, 33, 53]. This implies that the current passing through the barrier layer is nearly entirely ionic and the electronic current lies within the experimental error region of Faraday's law application for Al consumption, e.g. ±0.13% [33]. Also, the mechanism of ionic migrations during PAAF growth and related kinetic models, including only ionic currents, apply unhindered in various electrolytes and conditions [23, 54, 55]. This is valid even up to relatively high js, e.g. at least up to 35 mA cm^{-2} for H_2SO_4 at various temperatures [33].

The evolution at significant rates of molecular oxygen at ambient conditions in the oxide|electrolyte interface at pore bases (o|e) should retard or even block the mass and charge transport phenomena. Thus, PAAF growth should be retarded or even stopped. For example, at j = 10 mA cm^{-2}, taking that 0.1% of current is electronic then, at 1 atm and 298 K and per cm^2 of Al geometric surface, the rate of O_2 evolution must be ≈ 2.53 cm^3 s^{-1}. The porosity around pore bases equals the mean Al^{3+} transport number in barrier layer [56]. In 1.53 M H_2SO_4 electrolyte at j = 10 mA cm^{-2} and 298 K the porosity and transport number are ≈ 0.32 [33]; thus the real rate of O_2 evolution per cm^2 of pore base section surface is ≈ 8.43 cm^3 s^{-1}. For higher j = 35 mA cm^{-2} and equal percentage of electronic current 0.1% this rate becomes ≈ 2.53 × 3.5 = 8.86 cm^3 s^{-1}. At this j the above-mentioned transport number and porosity around pore bases are ≈ 0.22 [33], then the real rate per cm^2 of pore base section surface is ≈ 40.25 cm^3 s^{-1}.

It is hardly accepted that such high rates of oxygen volume evolution from pore bases would leave the mass and charge transport phenomena and the growth of PAAF unhindered or unblocked. Also, while oxygen evolution occurs, this evolution may not always be visually detected. A possible explanation would be that electronic current is in fact << 0.1 %, apparently not always true, and/or that, most likely, other phenomena still unknown prevent the visual detection and eliminate the hindrances to transport phenomena. The evolution of electronic current and oxygen is still an open research topic. Its elucidation is important and needs further experimental and theoretical work.

In this work Al is anodized in a suitable electrolysis setup to determine the region of j values where oxygen release is visually observed and the corresponding times at which its release is first visually detected. These are necessary to clarify the mechanisms of evolution of electronic current and oxygen. A novel mechanism is

proposed for the processes in the barrier layer that generate the electronic current and molecular oxygen, propagation of these processes and transfer of current. A mechanism is also given for the transport of oxygen as molecules and high-pressure nano-bubbles from pores, resulting in oxygen release that is visually detectable at suitable anodizing conditions. These mechanisms satisfactorily explain the results in this work and in the literature.

2. MATERIALS AND METHODS

Al specimens with thickness 0.5 mm, purity ≥ 99.95% (Merck pro-analysis), dimensions of conductive surface 3 × 3 cm^2, and total conductive surface area (S_g) 18.55 cm^2 were anodized. A Pb sheet of purity ≥ 99.968% (Merck pro-analysis) was used as cathode. The thickness, dimensions of conductive surface and total conductive surface area of Pb cathode were identical to those of Al. H_2SO_4 electrolyte solution at concentration (c_a) 5% w/v (or 0.51 M) was used. The temperature (T) was thermostatically adjusted to 298 (±0.1–0.2) K. Anodizing time (t) = 10 min and j = 1–100 mA cm^{-2} were employed. In preliminary experiments, the voltage vs. t plots [33] showed that the steady state stage of PAAF growth is reached at t < 10 min for $j \geq 2$ mA cm^{-2}.

In each experiment, fresh solution was used to avoid solution ageing. The entire procedure of Al specimen pre-treatment and anodizing were described in detail elsewhere [53-55]. Before Al anodizing experiments, the electrolyte solution was saturated with oxygen by blowing air, which had been previously purified by passing through a washer. Experiments were carried out after the complete relaxation of solution.

Water at 1 atm and 298 K saturated with air contains O_2 and N_2 at concentrations ≈ 9 ppm and ≈ 14 ppm, respectively, [57]. At such low concentrations, the concentration of each gas depends solely on its partial pressure and on Henry's law constant that depends on T. The saturation concentration of O_2 in pure water at 298 K and 1 atm O_2 is 31.6 cm^3 dm^{-3} [58]. From the molar volume (V_m) of ideal gases 24.4653 dm^3 mol^{-1} [58], this concentration is found to be ≈ 41 ppm. In 0.51 M H_2SO_4 solution at 298 K the saturation concentrations of O_2 in 1 atm air and pure O_2 may be a bit lower than 9 and 41 ppm. If pure O_2 gas at ambient conditions is evolved at pore bases, the concentration of O_2 everywhere in the solution around Al anode (anolyte) must be between 9 and 41 ppm. The initial saturation of solution with air minimizes or eliminates the absorption of released oxygen. Otherwise, its absorption could affect the results, leading to misleading conclusions.

Direct experimental observation of oxygen evolution within the pores is impossible. Observation is possible on Al anode surface and beyond it within the anolyte. In the used electrolytic cell setup, Figure 2, a glass tube open at both edges covers Pb cathode. Its lower edge is 5 cm below that of the Pb cathode. H_2 formed on the Pb surface [6] is directed upwards, remains in the tube and then is released out. The formed bubbles of H_2 do not mix with the solution outside the tube and therefore do not mix with the anolyte. Initially the solution was not stirred. But to avoid significant rise in temperature in the anolyte, the solution was later magnetically stirred at a rate suitable for each j that assures no-mixing of H_2 bubbles with anolyte. Only dissolved molecular H_2 can be

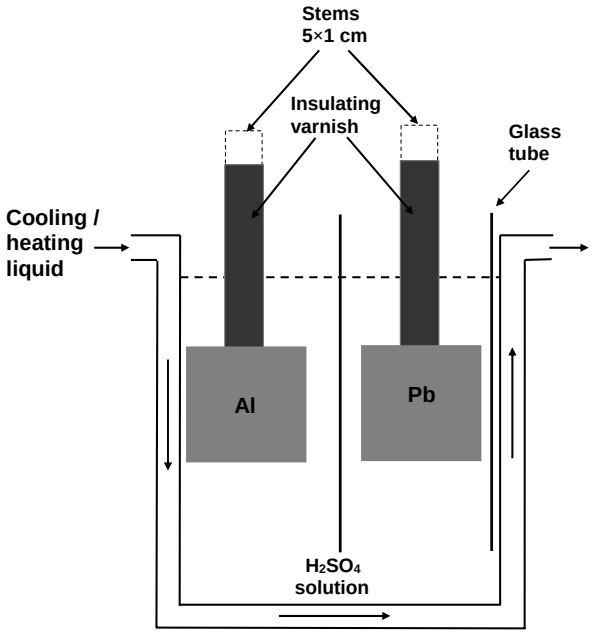

Figure 2. Electrolytic cell setup for Al anodization and observation of O_2 release on the Al anode surface.

transferred to the anolyte by diffusion and convection. Therefore, only oxygen gas release could be detected on the anode. H_2 solubility in water at 298 K and 1 atm H_2 is 19.1 cm^3 dm^{-3} [58] or ≈ 2 ppm. In the used solution it may be a bit lower. Thus, H_2 does not affect the observations on oxygen evolution in the anode.

Initially T was 298 K but, due to heat release and the required low stirring rate, T rises during anodizing. The Ts in the anolyte at t = 10 min are given in Table 1. Both faces of the Al anode surface were lit brightly and the release of oxygen was continuously observed by naked eyes and by magnifiers attached on cell walls. A method that combines the passing electric charge with Al consumption is commonly used in Al anodizing research. Al consumption is determined gravimetrically. Analytical balance has a sensitivity of 10^{-5} g or 10^{-4} g, so masses of released oxygen ≤ 10^{-5} g or 10^{-4} g, with corresponding volumes (at 298 K and 1 atm) ≤ 7.65 and 76.45 mm^3, cannot be determined gravimetrically. However, a bubble containing, e.g., even only 1 nano-mol oxygen (32×10^{-9} g) has volume ≈ 0.024 mm^3 and diameter ≈ 0.36 mm; thus the bubble can be visually detected. So, the method employed here can detect gas release at very low rates.

3. RESULTS AND DISCUSSION

3.1. Detection of oxygen gas release in the Al anode surface. Determination of related *j* boundaries

The summarized results on the release and detection of oxygen are given in Table 1. The time t_1 at which oxygen release is first detected decreases with j, Figure 3. The t_1 marks reversely the rate of oxygen evolution. Burning first appears at a j in the range 50-75 mA cm^{-2} and is probably closer to 75 mA cm^{-2}. For oxygen release during PAAF growth two j boundaries appear. The first is ≈ 10 mA cm^{-2} and the second is in the range 75-100 mA cm^{-2} and is probably closer to 100 mA cm^{-2}.

The denser oxygen release in the region of Al specimen surface from its middle to its upper edge, first seen at j = 35 mA cm^{-2}, and the general rise of local rate of oxygen release upwards for $j \geq$ 35 mA cm^{-2}, Table 1, are due to the distribution of local j in the Al surface [54, 59]. For non-stirred bath solution and low stirring rate, as the mean j increases and T decreases the local j along the Al surface increases upwards and its change from the bottom to the top widens [59].

For js below the upper j boundary, in addition to the release of visually seen oxygen gas bubbles, oxygen released in the forms of dissolved molecular oxygen and of smaller bubbles with sizes up to nm scale must also enter the bath solution. PAAFs usually grow at these js where the consumed Al tends to that determined by Faraday's law e.g. for H_2SO_4 and $H_2C_2O_4$ electrolytes [23, 31, 33, 53]. The overall rate of oxygen release (mol s^{-1}) is therefore low compared to the rate of Al consumption.

3.2. Generation and transfer of electronic current and generation of oxygen in the barrier layer region

The structure of PAAF around the barrier layer is defined by the surface density of active pores near Al surface (n), mean cell width (D_c) related to n by $4^{-1}\pi n D_c^{\,2} = 1$, mean interpore distance (D_{int}) = D_c/1.05, pore base diameter (D_p), and barrier layer thickness ($blt = 2^{-1}(D_c - D_p)/\sin\varphi$, Figure 1c). The ratio of real js in o|e and m|o interfaces is $j_{o|e}/j_{m|o} = (2blt\sin\varphi + 1)^2$. The φ and real m|o interface area are almost independent of electrolyte type and conditions [6]. But the o|e interface area varies significantly [33, 60]. The spherical sector surface area across the barrier layer falls and the local real j and field strength rise from m|o to o|e interface [34]. The partial cationic and anionic current densities increase exponentially with field strength [34]. Electronic current (e^- current) also obeys a complex exponential equation [46].

The anodic alumina at rest (after anodizing) is amorphous (am-Al_2O_3) [3, 4, 25]. Its lattice structure approaches that of γ-Al_2O_3 [3, 4]. The most stable α-Al_2O_3 has low standard formation enthalpy -1675.7 kJ mol^{-1} [57]. Formation enthalpy of γ-Al_2O_3 is 96.43% of that [58], while the enthalpy of am-Al_2O_3 must be only a bit higher than that of γ-Al_2O_3. Using the enthalpy of α-Al_2O_3 and the next processes together with their enthalpies [57], $Al_{(s)} \rightarrow Al_{(g)}$ (+326.4 kJ mol^{-1}), $O_{2(g)} \rightarrow 2O_{(g)}$ (+498.34 kJ mol^{-1}), $Al_{(g)} \rightarrow Al^{3+}_{(g)} + 3e^-$ (+5156.77 kJ mol^{-1}) and $O_{(g)} + 2e^- \rightarrow O^{2-}_{(g)}$ (+703 kJ mol^{-1}), lattice enthalpy is found to be 15498.55 kJ mol^{-1} using the Born-Huber cycle.

Table 1. Observations on the release of O_2 and related phenomena in the Al anode during electrolysis for 600 s at various current densities, j. The anodising voltage, ΔV, and temperature, T, at the end of experiments are also given.

J / mA cm^{-2}	Observations	Final ΔV / V	Final T / °C
1	No detectable release of oxygen.	5.8	25.2
2	No detectable release of oxygen.	8.3	25.5
5	No detectable release of oxygen.	14.5	26.2
10	Release of very small (just observable) and very sparse bubbles of oxygen on Al anode surface first observed at time t_1 towards the end of experiment, so $t_1 \approx 600$ s.[a]	18.4	27.3
15	Release of very small (just observable) and very sparse bubbles of oxygen on Al anode surface first observed at $t_1 \approx 480$ s.[a]	20.9	28.5
25	Release of very small (just observable) and very sparse bubbles of oxygen on Al anode surface first observed at $t_1 \approx 320$ s.[a]	23.2	29.5
35	Slightly faster release and higher surface density of oxygen bubbles. Bubbles first observed at $t_1 \approx 200$ s.[a] Denser release of bubbles in the middle of Al anode surface and upwards.[b]	24.5	32.0
50	Slightly faster release and higher surface density of oxygen bubbles than above. Bubbles first observed at $t_1 \approx 100$ s.[a,b]	25.4	35.5
75	Clearly faster formation of larger bubbles and at much higher surface density; thus significant rate of oxygen release but not massive release yet. Bubbles first observed at $t_1 \approx 30$ s.[a,b]. After the end of the experiment, small areas in the Al anode surface were observed where burning [55] occurred; thus non-uniform abnormal growth of PAAF took place. Burning is the phenomenon of much faster growth of PAAF that occurs locally and is linked with change in structural parameters of PAAF.	25.8	39.0
100	Initially, at $0 < t_1 \leq 5$ s, a clearly faster oxygen release started and a surface density of bubbles much higher than above appeared. Quickly after, a massive release of oxygen started from an upper corner at first. Afterward, oxygen release stopped while electropolishing phenomenon occurred producing a mirror-like surface. Next, in the other upper corner, similarly a massive oxygen release was observed first and then electropolishing occurred. A thin layer of solution in contact with Al anode surface was seen to flow downwards, like a waterfall. This is due to the strong changes in solution composition and density and presumably to an appreciable change in temperature thereto compared to the rest of the solution, so the local refractive index changes enabling the visual observation. Then, these also occurred in one of the two lower corners and then in the other. Electropolishing that started from the corners gradually spread over the entire surface. After anodizing, the electropolished surface was found to be highly conductive showing absence of developed insulating anodic oxide; thus there was only an ultrathin anodic oxide film or the naturally formed thin passive oxide layer.	26.1	42.5

[a]There was a tendency for the average size of released oxygen bubbles to increase with j.
[b]Detailed observations showed a general tendency for the local oxygen release rate to increase upwards along the Al anode surface.

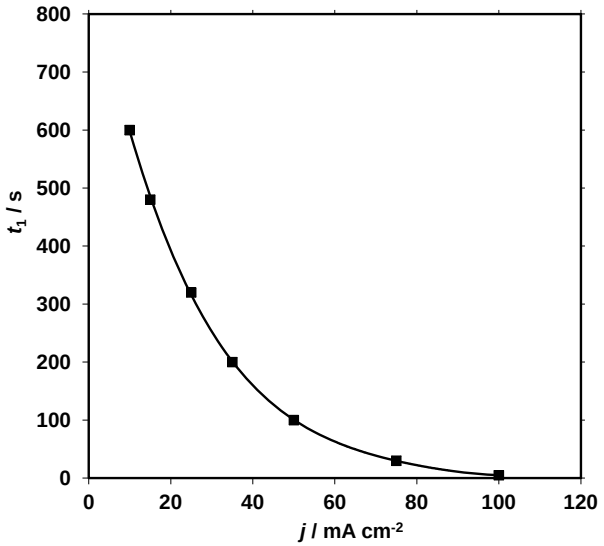

Figure 3. Variation of the time at which oxygen release is first detected on the Al anode surface, t_1, with current density, j.

Its high value agrees with predictions of the Born-Mayer equation [57]. This indicates a strong ionic bonding. Lattice enthalpies of γ- and am- are only a bit lower than that of α-Al_2O_3. In γ- and am-Al_2O_3 lattices, Al^{3+} ions occupy voids among O^{2-} in octahedral and tetrahedral vertices, respectively, [61]. Low formation enthalpy (< 0) and high lattice enthalpy (> 0) mark a highly stable lattice; thus the anodic alumina does not collapse under the action of the high-strength field during anodizing. Alumina has an energy band gap ≈ 7 eV [61] and is a dielectric material.

Because the PAAF and its barrier layer at rest are dielectric, the origin of e^- current during anodizing is a key query. It was related to the embodied electrolyte anions that behave as impurity centres [62] and as the primary source of avalanche e^- current through the oxide causing O_2 evolution [43, 45]. It was also ascribed to tunnelling effect [63].

Here, in H_2SO_4 electrolyte clear visible release of oxygen gas occurred at $j \geq 10$ mA cm^{-2}. In H_3PO_4 and mixtures of H_3PO_4 with other electrolytes at *T*s about the ambient temperature, clear visible release of oxygen was observed at 7 mA cm^{-2} [43, 45]. In $H_2C_2O_4$, gas release at significant rates in Al anode is visually seen at $T \geq 0$ °C and $j \geq 2.5$ mA cm^{-2} [23]. The *j* limit, above which gas release is seen, seems to depend mainly on the electrolyte type. For the main pore-forming electrolytes H_2SO_4, H_3PO_4 and $H_2C_2O_4$, gas release is seen visually above a *j* limit that decreases in this order. At given *j*, the gas release rate rises accordingly. The relative concentrations (wt%) of embodied electrolyte anions in PAAFs in these electrolytes [64] are as ≈ 4.63:3.17:1. In H_2SO_4 the concentration of anions and the *j* limit of oxygen release detection are highest; thus at given *j* the oxygen release rate is lowest. Embodied electrolyte anions do not seem to be the source of e^- current. Also, low rates of oxygen release could be attributed to tunnelling effect, but not the high ones observed e.g. at high *j*s. The results suggest a novel mechanism related to strong polarization of oxide-lattice and of its species.

During anodizing, under high field the barrier layer becomes mainly ionic and secondarily an electronic conductor. The field causes induced electronic polarization of single atoms, ions and molecules without permanent bipolar moment, polarization and bipolar orientation of species with such moment, and polarization of the entire ionic lattice so that the ion sites shift relative to those at rest [65]. The latter makes the lattice structure more open and plastic, allowing Al^{3+} and O^{2-} migration, and thus ionic conduction, and penetration of bulky anions such as sulphate with radius 0.242 nm [66].

The first electron affinity of O ($O + e^- \rightarrow O^-$) is -141 kJ mol^{-1} (exothermic) and the second ($O^- + e^- \rightarrow O^{2-}$) is 844 kJ mol^{-1} (endothermic) [57]. Though the state of O^{2-} in the barrier layer [3, 4, 6] differs from that of the free single O^{2-}, the affinities help to reveal the origin of e^- current. The second affinity is positive and high. Under high-strength field in the barrier layer, of the order 10^9 V m^{-1} [2-5], O^{2-} ions undergo polarization and destabilization, favoured by their medium charge and large radius, 0.140 nm, compared with the small radius of Al^{3+}, 0.053 nm [57]. Also, the outer lobular *p* orbitals in O^{2-} are receptive to field effect, much more than the inner spherical *s*. For each O^{2-} a small probability exists, depending on field strength, to become O^- ($O^{2-} \rightarrow O^- + e^-$); thus energy roughly -844 kJ mol^{-1} is removed. Then, $O^- \rightarrow O + e^-$ needing energy roughly 141 kJ mol^{-1}

<< 844 kJ mol^{-1} can occur. The charge of O^- is low but its radius 0.176 nm [58] is higher than that of O^{2-}. Repulsions among O^- and adjacent O^{2-} or O^- produce local swelling deformation but not collapse of lattice. The formed O has small radius, 0.48 nm [67] or 0.66 nm [68], producing local shrinkage deformation of lattice. The overall process $O^{2-} \rightarrow O + 2e^-$ is thus thermochemically prone and does not negate lattice stability.

The intraatomic, intraionic or intramolecular electric field strength is of the order 10^{11} V m^{-1} [65]. The mean field strength across the barrier layer is of the order 10^9 V m^{-1} [2-5]. The local field strength in it increases from m|o to o|e interface. If this would reach the intraionic field strength, the electronic structure of the ion should be completely destroyed. The applied field can only activate the detachment of up to two outer electrons from a few O^{2-} ions.

Electrons (e^-s) released could be captured from lattice Al^{3+} by the processes $Al^{3+} + e^- \rightarrow Al^{2+}$, $Al^{2+} + e^- \rightarrow Al^+$ and $Al^+ + e^- \rightarrow Al$ that are exothermic and thermochemically prone. Their energies are opposite to endothermic ionization ones ≈ 2744.6, 1816.6 and 577.4 kJ mol^{-1} [57]. But the overall process $Al^{3+} + 3e^- \rightarrow Al$ is related to a large increase in radius, from 0.053 nm [57] to 0.118 [67] or 0.121 [68], and hence to large swelling deformation of lattice towards its collapse. The Al^{3+} ions do not seem to partake in e^- current generation, which agrees with their weak polarization. A seeming contradiction appears: Under strong polarization, the release of two e^-s from O^{2-} occurs with energy removal, roughly ≈ -844 + 144 = - 703 kJ per 2 mol e^-s. But in alumina at rest, transfer of an e^- from the valence to conduction band needs energy > ≈ 7 eV [61], that is > ≈ 1350.79 kJ per 2 mol e^-s. The band structure and band gap of alumina at rest cannot justify e^- current generation in the barrier layer. But under high polarization, the energy bands change and shift strongly compared to those at rest and the mechanism of generation and transfer of e^- current also changes, elucidating this contradiction.

Within the barrier layer, O^{2-} ions are destabilized more and the probability of e^- generation rises as the local field strength increases from m|o to o|e interface [34]. The high electronegativity of O atom opposes e^- generation, and the related processes become reversible $O^{2-}{}_{latt} \leftrightarrows O^-{}_{latt} + e^-$, $O^-{}_{latt} \leftrightarrows O + e^-$ and $O^{2-}{}_{latt} \leftrightarrows O + 2e^-$ ($_{latt}$ means lattice). In oxide at rest, they shift completely to the left, so only O^{2-} ions exist. Under field action, they turn slightly to the right. Generation of e^-s also occurs in the m|o interface. The release of e^-s from O^{2-} may start in the m|o interface, followed by their transfer to Al conductor. Processes generating e^-s also occur in o|e interface. The continuation and thus the transfer of e^- current is possible by the above chain processes propagated inside the barrier layer. The change of field strength from m|o to o|e interface [34] ensures equal e^- current through each spherical-sector surface at each *t*. O atoms approach each other forming O_2 molecules and much less often O_3 [69], which fill voids and cavities in the lattice of solid oxide [45]. O_2 (or O_3) molecules are formed in the entire barrier layer and in the interfaces. In the following, when referring to oxygen gas, the contained small amount of O_3 is included.

If in the above processes ΔH_1, ΔH_2 and ΔH are the enthalpies, k_1, k_2 and k are the equilibrium constants and c_{O2-}, c_{O-} and c_O are the active concentrations (activities) of O^{2-}, O^- and O species, then $k_1 = c_{O-}/c_{O2-} = k_{1,0}\exp(-\Delta H_1/RT)$, $k_2 = c_O/c_{O-} = k_{2,0}\exp(-\Delta H_2/RT)$ and $k = c_O/c_{O2-} = k_0\exp(-\Delta H/RT)$, where $\Delta H = \Delta H_1 + \Delta H_2$ and $k_{1,0}$, $k_{2,0}$ and $k_0 = k_{1,0}k_{2,0}$ are constants independent of *T*. The $k_{1,0}$, $k_{2,0}$ and k_0 must depend and the ΔH_1, ΔH_2 and ΔH may depend on the local field strength. Considering, without compromising the reliability of analysis, that roughly $\Delta H_1 \approx$ -844 kJ mol^{-1} and $\Delta H_2 \approx$ 141 kJ mol^{-1}, then $-(\Delta H_1 + \Delta H_2) > 0$ and k decreases with *T*. Since $c_{O2-} >> c_{O-}$ and $c_{O2-} >> c_O$, the c_{O2-} is nearly constant and c_O decreases with *T*. This is valid also for the rate of oxygen release, explaining results quoted in section 1.

The validity of e^-/oxygen generation processes is then tested by their compatibility with all other known physicochemical processes in the barrier layer and by their ability to explain related results for various electrolytes.

3.3. Compatibility of electronic current and oxygen generation to physicochemical processes in the barrier layer

In the steady state stage of PAAF growth the mean transport numbers of O^{2-} and Al^{3+} ions in

the barrier layer, tn_{an} and tn_{ca} (tn_{an} + tn_{ca} = 1), are given by $tn_{an} = 1 - (D_p/D_c)^2$ and $tn_{ca} = (D_p/D_c)^2$ [51, 54], while tn_{ca} equals the porosity of film at pore bases [56]. They depend almost solely on T and j and trivially on electrolyte type [23, 33]. The tn_{an} (tn_{ca}) increases (decreases) with j and decreases (increases) with T. Al^{3+} ions are formed in the m|o interface, $Al \rightarrow Al^{3+} + 3e^-$, according to the total ionic charge passing and Faraday's law. The tn_{an} part of formed Al^{3+} ions is combined with O^{2-} ions that reach there to form oxide. Their tn_{ca} part migrates to the o|e interface and is ejected in the pore base solution. The O^{2-} ions are formed in the o|e interface and migrate to the m|o interface.

The O^{2-} ions are formed by the processes: (i) Dissociative adsorption of H_2O [25, 70] as OH^- and H^+ on Al^{3+} and O^{2-} lattice sites in oxide surface, $^{\cdots}Al^{3+\cdots}O^{2-\cdots} + H_2O \rightarrow {}^{\cdots}(Al^{3+\cdots}OH^-)\,{}^{\cdots}(OH)^{-\cdots}$, where $^{\cdots}$ is the dominant ionic bonding in the solid lattice. (ii) Under high field, the OH^- ions become strongly polarized and most of them decompose, $OH^- \rightarrow O^{2-} + H^+$; the produced H^+ ions are ejected in the pore base solution and the O^{2-} ions become new lattice sites [70], $^{\cdots}(Al^{3+\cdots}OH^-)^{\cdots}(OH)^{-\cdots} \rightarrow {}^{\cdots}(Al^{3+\cdots}O^{2-})^{\cdots}O^{2-\cdots} + 2H^+_{aq}$. The OH^- ions remaining in the outer sub-layer of barrier layer are also polarized and H^+ ions are finally detached and ejected. The sum (i) + (ii) gives $H_2O \rightarrow O^{2-}_{latt} + 2H^+_{aq}$.

Also, the processes generating e^-s/oxygen occur: (iii) $O^{2-}_{latt} \leftrightarrows O^{-1}_{lattice} + e^-$, $O^{-1}_{latt} \leftrightarrows O + e^-$ and $2O \rightarrow O_2$ (partly $3O \rightarrow O_3$), which are summed as $2O^{2-}_{latt} \rightarrow 4e^- + O_2$ (or $3O^{2-}_{latt} \rightarrow 6e^- + O_3$). The sum of $2O^{2-}_{latt} \rightarrow 4e^- + O_2$ and $H_2O \rightarrow O^{2-}_{latt} + 2H^+_{aq}$ gives: (iv) $2H_2O - 4e^- \rightarrow 4H^+_{aq} + O_2$, considered as the e^-/oxygen generation process [71]. So, (iv) is equivalent to (iii). Hence, the processes generating e^- current/oxygen are compatible with the rest in the barrier layer. The formulated mechanism of their generation is important and possibly applies to oxygen evolution in other oxides too [71].

Low e^- current means that at each t point a small portion of O^{2-}_{latt} partakes in e^-/oxygen generation and e^- transfer. The geometry of barrier layer, Figure 1, predicts that at given j the $j_{o|e}$ increases with blt. Also, the local spatial densities of O^- and O in barrier layer follow the local real j and field strength and increase from m|o to o|e interface. Molecular oxygen and oxygen-filled voids and nano-cavities (nano-bubbles) are formed with rising local spatial densities. Such voids and nano-cavities are enclosed in the barrier layer and pore walls, Figure 4a-b. When they are exposed to solution, oxygen is released. At pore bases this occurs because this layer advances to the Al side and the m|o and o|e interfaces are renewed, Figure 4a. In the remaining pore length this occurs because the pore walls gradually dissolve chemically and the pores widen slightly outwards, Figure 4b. Oxygen enters the pore filling solution as separate molecules and nano-bubbles. The rate of oxygen formation in o|e interface at pore bases (per unit of S_g or o|e area) must rise with blt. At given T, j and c_a, blt increases in the order H_2SO_4, $H_2C_2O_4$ and H_3PO_4 [3, 4, 7], explaining partly the more intense gas release in $H_2C_2O_4$ and H_3PO_4.

The rate of oxygen release as separate molecules and nano-bubbles at pore bases equals the rate of their formation in o|e interface + the rate of release of those enclosed in the barrier layer. The latter rate depends on their mean concentration in barrier layer up to a distance $D_p/2$ from pore axis, Figure 1c, and the rate of barrier layer renewal. PAAF thickness (h) obeys $h = k'jtn_{an}t$, where $k' = 6.9833 \times 10^{-5}$ cm^3 C^{-1} (constant) [33]. The renewal rate $k'jtn_{an}/blt$ is estimated e.g. for 1.53 M H_2SO_4, T = 298 K and j = 5-35 mA cm^{-2}, where tn_{an} = 0.64-0.79 and the steady state stage starts at t = 6.5-2.17 min with ΔV = 7.97–18.21 V [33]. The mean field strength is always ≈ 1 V mm^{-1}; thus roughly blt ≈ 7.97–18.21 nm. Then, the renewal rate is ≈ 0.28–1.06 s^{-1}. It also increases with j. Within Δt = 1 s a significant portion of molecular oxygen and nano-bubbles enclosed in the space up to a distance $D_p/2$ from pore axis is released or their total amounts enclosed in this space are released more than once.

The concentration of oxygen and its distribution in the pore walls affect the rate of oxygen release beyond pore bases, Figure 4b. This rate increases with h and the rate of oxide dissolution. For low c_as and not high ts, hs and Ts, as here, it is expected to be lower than the total rate of oxygen release at pore bases.

The formation of oxygen molecules and nano-bubbles, filling accordingly voids and cavities in the barrier layer, agrees with Al^{3+} and O^{2-} transport

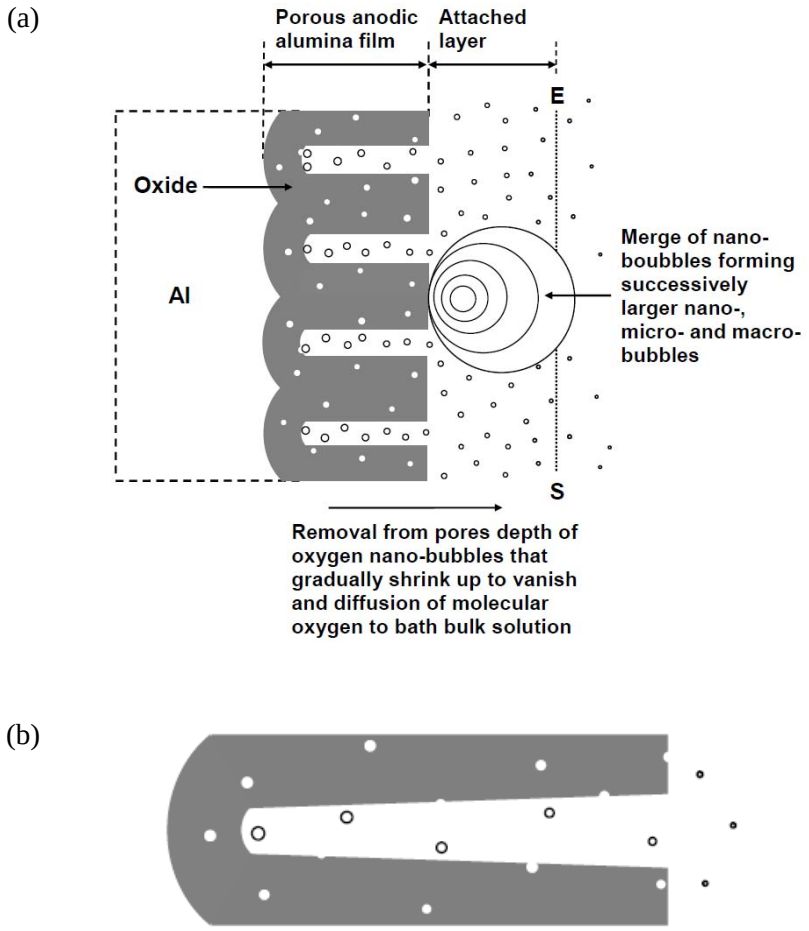

Figure 4. (a) Schematic representation of oxygen gas-filled cavities in the barrier layer and pore walls, and of oxygen nano-bubbles that entered the pore filling solution during PAAF growth. The nano-bubbles are removed from pore base, the dissolved molecular oxygen is diffused outwards and nano-bubbles merge in the attached layer region. As nano-bubbles move outwards, they gradually dissolve, shrink and vanish, or merge in the attached layer region. A PAAF of low thickness with cylindrical pores is assumed. (b) A cell unit of thicker PAAF with the pore opening outwards. Oxygen molecules and nano-bubbles enclosed in the pore walls are gradually exposed to the solution and enter it.

mechanism that includes clusters of Al^{3+} and O^{2-} ions [23]. Detachment of e^-s from O^{2-} cluster(s) and transport of Al^{3+} ions from nearest Al^{3+} cluster(s) produce voids or cavities filled with the oxygen formed.

3.4. Effect of the embodied electrolyte anions and other species on the generation of e^- current and oxygen

Species with clear permanent bipolar moment are mainly the embodied electrolyte anions. Due to their large size and low mobility and concentration, their role in ionic conduction is marginal, in contrast to O^{2-} and Al^{3+} that migrate at high rates. Also, their polarization can contribute to e^- current/oxygen generation, but only in cases where they decompose.

At given T, j and c_a, the increase in *blt* in the order H_2SO_4, $H_2C_2O_4$ and H_3PO_4 [3, 4, 7] means increase of e^- current and of oxygen evolution rate also, at least at pore bases. But, as noted earlier, the rate of gas evolution is reversed for $H_2C_2O_4$ and H_3PO_4. The formation enthalpies of SO_4^{2-}, PO_4^{3-} and $C_2O_4^{2-}$ are -903.7, -1245.2 and -845.2 kJ mol^{-1} [72]. Due to low enthalpy value (< 0) and tetrahedral compact structure of SO_4^{2-} and PO_4^{3}

these are stable, which is valid also for HSO_4^-, $H_2PO_4^-$ or HPO_4^{2-} possibly present in the barrier layer. For $C_2O_4^{2-}$, the enthalpy is higher and the structure is open. Its strong polarization breaks the C-C bond with intermediate strength (bond enthalpy (≈ dissociation energy) = 348 kJ mol^{-1} [57]) and the process $C_2O_4^{2-} \rightarrow 2CO_2 + 2e^-$ takes place. Embodied $HC_2O_4^-$ also decay, $HC_2O_4^- \rightarrow CO_2 + CO + OH^-$, and the OH^- ions finally decompose to O^{2-}_{latt} and H^+_{aq}. These O^{2-}_{latt} ions are a tiny fraction of O^{2-}_{latt} in the barrier layer. The e^-s and O^{2-}_{latt} thus formed are assimilated by the processes (iii). The decay of oxalate anions also explains their lower concentration in oxide than that of sulphate and phosphate [64].

The rate of release of oxygen + CO_2 + CO exceeds that of oxygen. If oxalate anions did not decay, the gas release rate would rise in the order H_2SO_4, $H_2C_2O_4$ and H_3PO_4. But they decay and the order is reversed for $H_2C_2O_4$ and H_3PO_4. The generation of e^- current and oxygen coming from oxalate anions is thus related to their decay. Any other effect of each type of electrolyte anion on their generation is indirect, possibly mainly through further deformation of the lattice.

The O_2 molecules formed can be polarized, but due to strong O=O bond (enthalpy 498.34 kJ mol^{-1} [57]) these do not seem to decay. The bent O_3 molecule has two weaker resonance bonds, among the central O atom and the side ones, each with enthalpy ≈ 219 kJ mol^{-1} that is ≈ 1.5 times the enthalpy of single bond 146 kJ mol^{-1} [57]. O_3 can partly give O_2 + O and an equilibrium process may appear. Due to tiny O_3 amount, the processes (iii) remain almost unaffected.

3.5. The states of oxygen in the pore filling solution, attached layer and bath bulk solution

A relatively immobile attached layer adheres by adsorption forces on Al anode surface. It extends up to the imaginary surface ES, Figure 4a. Its thickness is up to the order of 100 μm [73] and depends on solution type, T and stirring rate.

After the nucleation and during the growth of pores, oxygen molecules and nano-bubbles that are released in the pore filling solution dissolve rapidly. This solution becomes saturated with dissolved oxygen at concentration near 41 ppm, starting from pore bases. A gradient of oxygen concentration along the pores and across the attached layer is also created, allowing oxygen to diffuse outwards. Beyond ES surface, its concentration is almost constant, close to 9 ppm. After saturation of pore filling solution, nano-bubbles that enter it remain for a finite time, Figure 4a-b, and further change the concentration of dissolved oxygen. The solution that fills the growing pores forces nano-bubbles to move outwards.

Nano-bubbles of mean diameter D are assumed to enter the base of pores. D_p and n are ≈ 10–100 nm and ≈ 10^9–10^{11} cm^{-2}, respectively, for different electrolytes and conditions [7, 51]. For normal PAAF growth in H_2SO_4 and js applied here, D_p varies from about ten up to a few tens of nm and increases with j, while n is of the order 10^{10} cm^{-2} and decreases with j [5, 7]. Due to widening of pores outwards, Figure 4b, oxygen molecules and nano-bubbles enclosed in pore walls are gradually released.

Inside any cavity filled with molecular O_2 (bubble) in the solution the pressure is given by the Laplace equation [57]

$$P_{in} = P_{out} + 2\gamma/(D/2) \quad (1)$$

where γ is the surface tension of solution in the pores. Because c_a is low, γ can be taken to be approximately that of H_2O [58], that is 72.0 × 10^{-3} N m^{-1} at 298 K [57]. For ease, it is always considered that T = 298 K, without damaging the analysis. The critical pressure, temperature and molar volume of O_2 are P_c = 50.14 atm, T_c = 154.8 K and V_c = 78 cm^3 mol^{-1} [57]. The reduced parameters $P_r = P_{in}/P_c$, $T_r = T/T_c$ and $V_r = V_m/V_c$ obey the van der Waals equation [57]

$$P_r = 8T_r/(3V_r - 1) - 3/V_r^2. \quad (2)$$

P_{in}, P_r, T_r, V_r, V_m and density of O_2 (d) were found for D = 0.5 mm (macro-bubble) and D = 1-100 nm (nano-bubbles), Table 2. As D decreases, d increases. When D approaches 1 nm, d tends to that of water or solution. Henry's law

$$P_{in} = k_1 x, \quad (3)$$

where k_1 is constant depending on T (and as expected partly on c_a) and x is the O_2 concentration (molality) in the solution, describes the pressure

of O_2 in a bubble as a function of O_2 saturation concentration in the solution around it in equilibrium, Figure 5a. For the used solution, k_1 must be close to that of water 7.92×10^4 kPa kg mol^{-1} at T = 298 K [57].

For D = (0.5 mm)–(1 nm), x = 0.001–3.638 mol kg^{-1}, Table 2. As D decreases, P_{in} and x increase. The nature of Henry's law is thermodynamic. It applies to macroscopic and microscopic systems but, reasonably, it does not apply so satisfactorily in nanoscopic systems. For low Ds of the order of nm, the high x and its large changes imply a change in k_1, so the results are not precise enough. P_{in}s are valid for Ds $\geq \approx$ 10 nm [74]. A bubble

Table 2. Values of O_2 bubble diameter, D, and of the corresponding pressure, P_{in}, reduced pressure, P_r, reduced temperature, T_r, reduced molar volume, V_r, density of O_2 in the bubble, d, saturation concentration of O_2 in the solution around the bubble at static conditions, x_{O2}, and number of O_2 molecules in the bubble, N (bubble). The number of O_2 molecules in a spherical cavity with diameter D formed inside the oxide, from which all the previously contained Al^{3+} ions migrated and the O^{2-} ones became O_2, N (cavity), is also given. The calculations were made at temperature 298 K.

D	P_{in} / atm	P_r	T_r	V_r	V_m / cm^3	d / g cm^{-3}	x_{O2} / mol kg^{-1}	N (bubble)	N (cavity)
0.5 mm	1.01	0.02	1.93	255.69	19943.82	0.002	0.001	≈ 2E+15	≈ 1.3E+18
100 nm	29.42	0.59	1.93	8.50	663.29	0.048	0.038	475137	10566839
10 nm	285.23	5.69	1.93	0.86	67.10	0.477	0.365	4697	10567
5 nm	569.47	11.36	1.93	0.59	46.06	0.695	0.729	855	1321
2 nm	1422.17	28.36	1.93	0.45	35.31	0.906	1.819	71	85
1 nm	2843.34	56.71	1.93	0.40	31.32	1.022	3.638	10	11

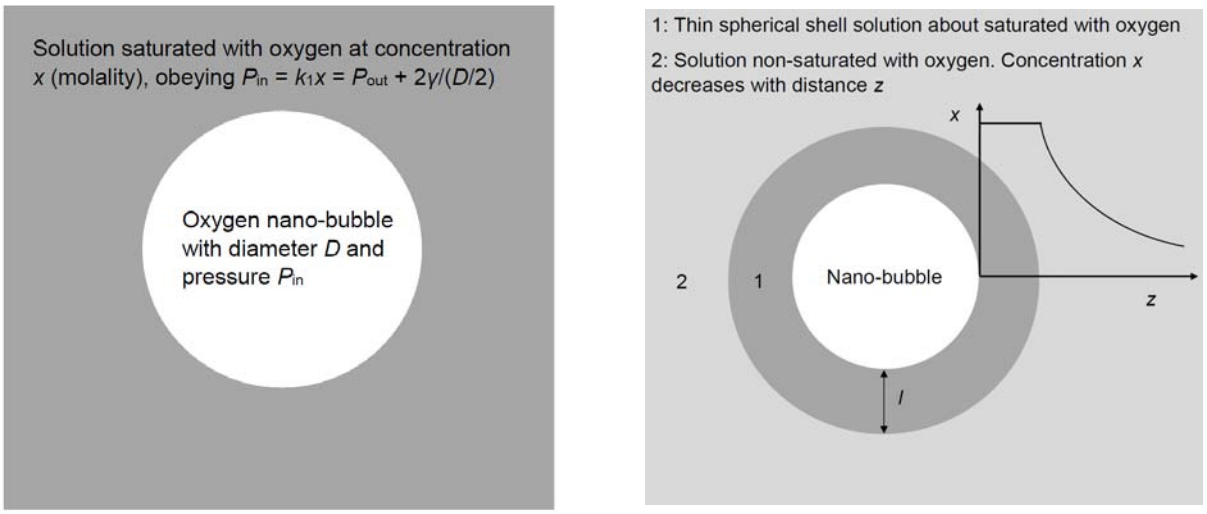

(a) (b)

Figure 5. (a) Nano-bubble in equilibrium with the entire surrounding solution under static conditions. (b) Under non-static conditions the nano-bubble is in about equilibrium with a spherical-shell thin-layer-solution around it, beyond which the concentration of dissolved oxygen decreases radially with distance.

contains $N = (4/3)\pi(D/2)^3 V_m^{-1} N_A$ number of O_2 molecules, where N_A is the Avogadro constant, Table 2. Thermodynamic analysis of a system normally premises a number of species of order 10^4 and above. This about agrees with analysis validity up to D = 10 nm [74]. For D < 10 nm, the bubble deviates from such a system. Results at $D \geq 10$ nm are quantitatively acceptable. Results at D < 10 nm describe mostly qualitative trends. Accurate results require the involvement of the unknown activities instead of P_{in} and x. From Eqs. (1) and (3)

$$k_1 x = P_{out} + 2\gamma/(D/2), \quad (4)$$

which relates x to D. At static conditions, an equilibrium is set up among high-pressure O_2 in nano-bubble and dissolved O_2 around it, Figure 5a. As O_2 diffuses outwards, this is in fact a quasi-equilibrium, Figure 5b. The x in a thin-spherical-shell solution of thickness l around nano-bubble is in about equilibrium with P_{in}, or with D, and rises as D decreases until the bubble is exhausted and disappears. Outside the shell, x decreases radially with z. For more than one nano-bubble in a finite space, x between and beyond them depends in a complex way on their spatial density and distribution, D, t, T, etc.

An oxygen-filled cavity in the barrier layer results from the migration of the previously contained Al^{3+} ions, and the conversion of corresponding O^{2-} to oxygen gas. Thus, a spherical cavity contains $N = (4/3)\pi(D/2)^3 d_c MM^{-1} N_A$ number of O_2 molecules, where d_c = 3.42 g cm^{-2} is the density of compact oxide [59] and MM is the molar mass of oxide. At given D, it exceeds the N in the bubble, more for higher Ds, Table 2. P_{in} in the cavity is thus higher. When opened and exposed to the solution, a larger bubble or some smaller ones are released. The size of cavities is a few nm to a few tens of nm [45], but in other cases it is smaller. For each low D, the above Ns do not differ much. When the cavity is opened, the expansion of released bubble is limited. Large expansion inside the pores, e.g. at a pressure approaching 1 atm, will block the anodizing process. However, such a blockage was not observed. The nano-bubbles present in the pore filling solution make it contain oxygen at high concentration without interrupting the process.

3.6. The mechanism of oxygen transfer from the pores and development of visible bubbles on Al anode surface

The oxygen of a single nano-bubble in a pore steadily dissolves in the spherical shell solution, where $x \approx k_1^{-1} P_{in} = k_1^{-1}[P_{out} + 2\gamma/(D/2)]$, from which it diffuses radially, Figure 5b. The diffusion rate (mol s^{-1}) at distance z is $-D_{diff} A d_s dx/dz$, where D_{diff} is diffusion coefficient, d_s is solvent density and A is spherical surface $\pi(D + 2z)^2$. Oxygen transfer from a bubble is related to the increase of P_{in} and $x_{z=0}$ and decrease of D and $(dx/dz)_{z=0}$ (<0), while d_s may vary with t and z but at first approach it is taken constant. Oxygen mass in the bubble $(4/3)\pi(D/2)^3 V_m^{-1}$ also decreases, Table 2, as expected.

Mass balance at z = 0 gives $d[(4/3)\pi(D/2)^3 V_m^{-1}]/dt = d\{(4/3)\pi x d_s[(l + D/2)^3 - (D/2)^3]\}/dt - D_{diff} A_{z=0} d_s (dx/dz)_{z=0}$, or $d[(4/3)\pi(D/2)^3 V_m^{-1}]/dt = d\{(4/3)\pi k_1^{-1}[P_{out} + 2\gamma/(D/2)] d_s[(l + D/2)^3 - (D/2)^3]\}/dt - D_{diff}\pi(D+2l)^2 d_s (dx/dz)_{z=0}$. The three terms are the rates of oxygen removal from bubble, its accumulation in the spherical shell and its transfer by diffusion. A similar complex equation can be formulated for z > 0. Their solutions require numerical methods. As a nano-bubble moves outwards, the final result is the transfer of oxygen outwards and disappearance of nano-bubble in the pore, attached layer, or bulk solution. The detailed study of related transport phenomena goes beyond the scope of the current study. For more nano-bubbles in a cylindrical pore, the mean local concentration of dissolved oxygen and the number of nano-bubbles decrease outwards.

The driving forces for oxygen transfer are: (i_1) The difference between high concentration of dissolved oxygen at pore depth and ≈ 9 ppm beyond ES, Figure 4a. (ii_1) The increase in P_{in} in the shrinking nano-bubbles until their vanishing.

Some large nano-bubbles, destined to disappear beyond ES, accumulate in the attached layer. Their local mean spatial density and D (c_{al} and D_{al}) change with t until c_{al} reaches a critical value, depending on D_{al}. Then, an avalanche-like merger of nano-bubbles is triggered. These approach each other and the spherical shells saturated with dissolved oxygen come into contact. Because x is higher for smaller nano-bubbles, oxygen is

transferred from small to large ones. Thus, they merge, Figure 4a, serially into larger nano-, micro- and maybe macro-bubbles that are first seen at t_1, Table 1.

P_{in} and T in the growing macro-bubble do not differ appreciably from 1 atm and 298 K. But V_m, Table 2, is appreciably lower than that of ideal gases 24.4653 dm^3 mol^{-1} [58]. The Eq. (2) applies approximately to the real gases, the molecules of which are subject to molecular interactions. Even if the real difference is smaller, this does not affect the analysis.

When N' nano-bubbles, each with a molar volume $V_{m,n}$, merge into a micro- or macro-bubble of diameter D_b and with a molar volume $V_{m,m}$, the mass balance $(4/3)\pi(D_b/2)^3/V_{m,m} = N'(4/3)\pi(D/2)^3/V_{m,n}$ gives $D_b = N'^{1/3}(V_{m,m}/V_{m,n})^{1/3}D$. Since $V_{m,m} >> V_{m,n}$, Table 2, the bubble of diameter D has a volume $V_{m,m}/V_{m,n}$ times that of all N' nano-bubbles. As P_{in} decreases, the solution near the bubble becomes supersaturated, $x_{O2} > P_{in}/k_1$, that further feeds the growing bubble and its expansion. In a pore, the occasional entry of a nano-bubble with $D \geq D_p$, or merging of nano-bubbles into such large nano-bubbles, may stop the anodizing until the bubble dissolves, becomes smaller in size and the anodizing is restored.

An expanding bubble encounters adjacent nano-bubbles that are also merged and an avalanche-like or blast expansion keeps on. After the merger starts, visually detectable bubbles may be soon formed, or t_1 is close to the start time. When the buoyancy surpasses the gravity together with attachment forces, the bubble comes off. As these forces depend also on the volume of the bubble, this remains attached up to a size limit, generally different for various surface positions.

At given c_a, T and t, as j increases the evolution of oxygen and formation of nano-bubbles become faster. Thus, macro-bubbles appear earlier and are denser on Al anode surface. Oxygen molecules and nano-bubbles also enter the bath bulk solution at higher rates. If nano-bubbles enter the pores at a rate below a limit, depending on their size, the critical c_{al} in the attached layer is not reached until 600 s, as Figure 3 predicts. Oxygen evolution in both forms also occurs at js < 10 mA cm^{-2} but, as the nano-bubbles move outwards, all of or part of them dissolve completely. Therefore, the critical c_{al} is not reached. Due to high field strength in the barrier layer, oxygen evolution occurs at all js of PAAF growth. At low and intermediate js, e^- current is really tiny. Its exact fraction is another open research topic. Quantitative structural and kinetic parameters, such as D_b, n, h or pore length, porosity etc., are not involved in the introduced novel mechanisms of generation, transport and release of e^-s and oxygen. The detailed related analysis needs further specific work.

The H_2 molecules formed on Pb cathode surface, Figure 2, also enter the catholyte or form bubbles that are released and small ones that enter it and dissolve. Only H_2 molecules can reach the anode, so the release of oxygen is not affected.

The strong disinfectant effect of electrochemically treated water using Ti electrodes [69] is now explained. Ti anodizing also produces barrier-type or porous-type oxide films [1, 3]. Similar mechanisms must govern oxygen evolution and transfer. Nano-bubbles and the higher concentration of dissolved O_2 and O_3 give water a high disinfectant effect.

Using PAAF as a mold, nano-porous anodes for only oxygen evolution can be developed. The oxide from the pore base up to the Al surface can be removed [7]. A thin layer of non-anodically oxidized metal, such as Au, deposited on the pore walls and bare Al surface allows oxygen evolution throughout the surface of pores. Polarized/charged metal surface atoms act as cations. Following (i) + (ii) process, an O^{2-} layer is electrochemically adsorbed which can produce e^-s and oxygen. Other reaction paths may be possible too. In suitable electrolytic cell and conditions, formation and storage of ultra-dense O_2, as nano-bubbles + dissolved O_2 in equilibrium, are possible by controlling oxygen release into the atmosphere. Co-product O_3 makes this oxygen system a strong oxidizing and disinfecting agent [69, 75].

3.7. The effect of oxygen gas evolution on the nucleation and growth of PAAF nanostructures

The e^- current is negligible compared to the ionic [31, 33, 53], so its inclusion in the kinetics of normal PAAF growth is needless [54, 55]. But the oxygen-filled voids and nano-cavities formed

during anodizing [45] affect the primary and secondary structure of oxide. Also, the generation of e^-s/oxygen affects the nucleation and growth of porous structure.

Oxygen-filled voids and cavities in the barrier layer when exposed to o|e interface at pore bases are filled with solution and the oxygen is removed, Figure 4a. Depending on their geometry and depth, the cavities can become pore nuclei, Figure 6. They can cease growing, or turn into pores that grow along with the older ones from which they stem and thus new pores appear. The new pores can continue to grow alongside the older, or be favoured to assimilate older pores, or later stop growing. Thus, incessant generation and termination of nuclei/pores occur [51], more at higher *j*s where the rate of oxygen evolution is also higher. In certain anodizing conditions, the generation and termination of new pores may be repeated periodically, so a serrated structure that is usually associated with oxygen evolution appears [44, 48-50]. Also, this structure may grow almost unidirectionally with an inclination to the pore axis [44, 48-51].

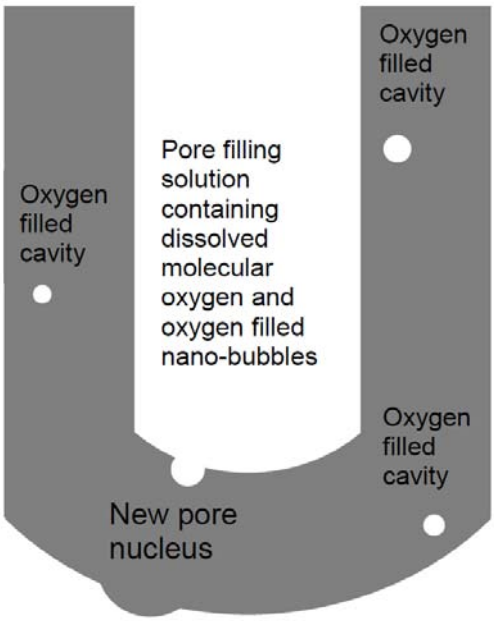

Figure 6. Formation of a pore nucleus at pore depth when an embodied oxygen-filled cavity is exposed to the solution at pore base. The oxygen is removed and the cavity is filled with solution. The nucleus can degenerate, or grow into a new pore as an inward-directed branch.

Oxygen evolution changes n (hence D_c and D_{int}) through the prevailing generation or termination of pores [51, 54]. The mean D_p and *blt* obey PAAF growth kinetics [6], determined by c_a, T, j, anodic potential (P_{an}), ΔV etc. The composition of solution inside the pores changes during their elongation. Al^{3+} ions ejected by the field at pore bases and those formed by dissolution of pore walls form colloidal particles made of Al^{3+}, electrolyte anions, H_2O and OH^- [76] and complex cations [77, 78] less mobile than H^+ [72]. Their concentrations are highest at pore bases. The real anodizing temperature in barrier layer, which exceeds T even slightly [53], also increases with t or h. They affect the composition and thickness of barrier layer, field strength and real j in it and thus the generation of e^-s and oxygen. The rate of oxygen evolution at pore bases, size of nano-bubbles etc. change too. The rate and mode of generation/termination of pores can thus vary with P_{an} or ΔV, partly determining the multimodal dependence of PAAF structural features on P_{an} or ΔV [6].

Modulated pores [47, 50, 79], formed by two- or three-step anodizing in different electrolytes or concentrations, were also related to oxygen evolution [47]. At given T, the ΔV or P_{an} may be regulated to give identical n, D_c and D_{int} of self-organized pores in the first region of steady state stage where they remain almost stable for each electrolyte. Then, D_p and j vary with electrolyte type, and the modulated structure is sufficiently explained mainly by the change in tn_{ca} [51]. At given T and j but with different electrolytes, in one-step anodizing, the mean n, D_c, D_{int} and D_p of self-organized pores in that region generally differ. So, they tend to change with each successive step. Besides tn_{ca}, oxygen evolution, real anodizing temperature and predominant generation or termination of pores affect the modulated structure in a more complex way.

The significant rate of oxygen release at j = 75 mA cm^{-2}, Table 1, implies a local dense-active-branching of pores inwards related to burning. Branching increases the mean local n and reduces D_c, D_p and *blt* [6, 51, 54]. The m|o interface area is nearly constant [6] and in burning region the

o|e interface area approaches the m|o interface area. For an applied ΔV (or P_{an}), lower local *blt* means higher mean field strength in the barrier layer and higher local *j*. Due to constant current jS_g, the mean *j* in the surface area where normal growth of PAAF occurs is lower. The rate of oxygen evolution increases with *blt* and mean field strength and real *j* in the barrier layer. So, the rates of oxygen evolution in the surface area where normal growth of PAAF occurs and in the surface area where burning appears do not differ exceedingly. The current jS_g is distributed in these two areas; thus burning can occur only in a limited part of S_g. After its start, an almost steady state is soon established in each area.

At j = 100 mA cm^{-2} the mean field strength in the barrier layer is higher and intense oxygen evolution initially occurs, producing dense branching of pores inward. Also, the real anodizing temperature rises significantly with *t*. Both favor the limiting case $D_c - D_p \rightarrow 0$, or $D_p/D_c \rightarrow 1$, or $tn_{ca} \rightarrow 1$. The array of barrier layer units is then transformed into an ultra-thin, almost flat barrier-type film. O^{2-} and Al^{3+} ions in appropriate proportions exist as an almost-atomic layer on the surface of Al. Al^{3+} ions are ejected into the solution at high rate and O^{2-} ions are involved in the fast generation of e^-s and massive release of oxygen. As the temperature rises further, practically $tn_{ca} = 1$. Then, electropolishing [8] is the only process that occurs, which is an almost direct ejection of Al^{3+} from Al surface into the solution at faradaic rate.

4. CONCLUSIONS

From the results and analysis of this work the following concluding remarks can be drawn:

1. In the applied electrolysis conditions, the release of O_2 in the Al anode is visually detected above a current density boundary. Its release is enhanced and starts earlier with increasing current density, but remains mildly detectable up to a much higher second boundary. Below it, the normal growth of PAAF is transformed to abnormal so that local burning appears on the Al anode surface. Above it, serially in time, intense and massive release of oxygen and electropolishing occur.

2. A novel mechanism for the generation of e^- current and oxygen is proposed, based on certain processes that are activated by the high field in the barrier layer and thermochemically prone. These come from the polarization of lattice O^{2-} ions under the action of high field, $O^{2-} \leftrightarrows O^{-1} + e^-$ and $O^{-1} \leftrightarrows O + e^-$ followed by $2O \rightarrow O_2$ (partly $3O \rightarrow O_3$).

3. Oxygen is formed inside the barrier layer and in the m|o interface that is embodied as separate molecules and nano-bubbles filling voids and cavities, respectively. They are also formed in the o|e interface and enter directly the pore base solution. Oxygen embodied in the barrier layer up to a distance $D_p/2$ from pore axis is released at pore bases as this layer is continuously renewed and that embodied in pore walls is released later by their chemical dissolution. The nano-bubbles contain high-pressure ultra-dense oxygen.

4. A novel mechanism for oxygen transfer is also proposed. In a spherical-shell solution-layer around each separate nano-bubble in the pore, a saturation concentration of oxygen is established. It is many orders of magnitude higher than that in air and pure oxygen in ambient conditions. This dissolved oxygen diffuses radially enriching the pore filling solution. An outward decrease of the mean local concentration of dissolved oxygen is fast set up, ensuring the transfer of oxygen from pore base, and generally from pore, to the attached layer and bath solution. The nano-bubble shrinks followed by the increase in its pressure and in oxygen concentration in the spherical shell, until the bubble vanishes in one of these spaces.

5. Nano-bubbles can gradually accumulate in the attached layer; then their merging occurs like an avalanche or blast. In the growing bubble the pressure falls and the volume expands. The growing bubble becomes a larger nano-bubble or a micro-bubble and possibly a macro-bubble that is visually observable.

6. The mechanisms of generation of e^- current and oxygen in the barrier layer and transfer of oxygen satisfactorily explain the present results and the literature ones on O_2 evolution during PAAF growth. They can also be applied to oxygen evolution in other oxide-coated anodes. The serrated structures of PAAFs, the branching of

pores inwards and the incessant generation and termination of pores are explained by the generation of e^- current and oxygen and the related mechanism. The multimodal dependence of structure on the anodizing potential and the modulated pores are also partly explained. These mechanisms are therefore a vital part of the overall PAAF growth mechanism.

7. The entry of oxygen nano-bubbles in the liquid phase results in high concentration of oxygen content while the external pressure is low. Using PAAF as a mold, functional nano-materials can be formed to be used as anodes suitable to produce and store oxygen only, as nano-bubbles and dissolved molecular oxygen at high concentration. The expected formation of co-product O_3, expands the applications of this oxygen system as a strong oxidising and disinfecting agent.

CONFLICT OF INTEREST STATEMENT

The author declares no conflict of interest.

REFERENCES

1. Lee, W. and Park, S. J. 2014, Chem. Rev., 114(15), 7487.
2. Keller, F., Hunter, M. S. and Robinson, D. L. 1953, J. Electrochem. Soc., 100(9), 411.
3. Young, L. 1961, Anodic Oxide Films, Academic Press, London.
4. Diggle, J. W., Downie, T. C. and Goulding, C. W. 1969, Chem. Rev., 69(3), 365.
5. Patermarakis, G. and Moussoutzanis, K. 2011, J. Electroanal. Chem., 659(2), 176.
6. Patermarakis, G. 2020, Curr. Top. Electrochem., 22, 1.
7. Sulka, G. D. 2008, Nanostructured Materials in Electrochemistry, A. Eftekhari, Ed., John Wiley and Sons, Wienheim, p. 1.
8. Sheasby, P. G. and Pinner, R. 2001, The Surface Treatment and Finishing of Aluminum and Its Alloys, ASM International & Finishing Publications Ltd., USA-UK.
9. Martin, C. R. 1996, Chem. Mater., 8(8), 1739.
10. Kovtyukhova, N. I. and Mallouk, T. E. 2005, Adv. Mater., 17(2), 187.
11. Ganley, J. C., Riechmann, K. L., Seebauer, E. G. and Masel, R. I. 2004, J. Catal., 227(1), 26.
12. Pellin, M. J., Stair, P. C., Xiong, G., Elam, J. W., Birrell, J., Curtiss, L., George, S. M., Han, C. Y., Iton, L., Kung, H., Kung, M. and Wang, H. H. 2005, Catal. Lett., 102(3-4), 127.
13. Burgos, N., Paulis, M. and Montes, M. 2003, J. Mater. Chem., 13(6), 1458.
14. Das, G., Patra, N., Gopalakrishnan, A., Zaccaria, R. P., Toma, A., Thorat, S., Di Fabrizio, E., Diaspro, A. and Salerno, M. 2012, Analyst, 137(8), 1785.
15. Toccafondi, C., La Rocca, R., Scarpellini, A., Salerno, M., Das, G. and Dante, S. 2015, Appl. Surf. Sci., 351, 738.
16. Jessensky, O., Muller, F. and Gösele, U. 1998, Appl. Phys. Lett., 72(10), 1173.
17. Zhang, L., Cho, H. S., Li, F., Metzger, R. M. and Doyle, W. D. 1998, J. Mater. Sci. Lett., 17(4), 291.
18. Jessensky, O., Muller, F. and Gösele, U. 1998, J. Electrochem. Soc., 145(11), 3735.
19. Nielsch, K., Choi, J., Schwirn, K., Wehrspohn, R. B. and Gösele, U. 2002, Nano Lett., 2(7), 677.
20. Li, A. P., Muller, F., Bimer, A., Nielsch, K. and Gösele, U. 1998, J. Appl. Phys., 84(11), 6023.
21. Li, A. P., Müller, F. and Gösele, U. 2000, Electrochem. Solid-State Lett., 3(3), 131.
22. Napolskii, K. S., Roslyakov, I. V., Eliseev, A. A., Petukhov, A. V., Byelov, D. V., Grigoryeva, N. A., Bouwman, W. G., Lukashin, A. V., Kvashnina, K. O., Chumakov, A. P. and Grigoriev, S. V. 2010, J. Appl. Crystallog., 43(3), 531.
23. Patermarakis, G. and Diakonikolaou, J. 2012, J. Solid State Electrochem., 16(9), 2921.
24. O'Sullivan, J. P. and Wood, G. C. 1970, Proc. Roy. Soc. Ser. A. Math. Phys. Sci. 317(1531), 511.
25. Patermarakis, G. and Kerassovitou, P. 1992, Electrochim. Acta, 37, 125.
26. Thompson, G. E. and Wood, G. C. 1981, Nature, 290, 230.
27. Thompson, G. E. 1997, Thin Solid Films, 297, 192.
28. Lee, W., Ji, R., Gösele, U. and Nielsch, K. 2006, Nat. Mater., 5, 741.

29. Li, F., Zhang, L. and Metzger, R. M. 1998, Chem. Mater., 10, 2470.
30. Masuda, H., Hasegwa, F. and Ono, S. 1997, J. Electrochem. Soc., 144, L127.
31. Patermarakis, G. 2009, J. Electroanal. Chem., 635, 39.
32. Patermarakis, G. 2009, Mat. Sci. Ind. J., 5(4), 364.
33. Patermarakis, G. and Moussoutzanis, K. 2009, Electrochim. Acta, 54(9), 2434.
34. Patermarakis, G., Karayianni, Ch., Massavetas, K. and Chandrinos, J. 2009, J. Solid State Electrochem., 13, 1831.
35. Garcia-Vergara, S. J., Skeldon, P., Thompson, G. E. and Habazaki, H. 2006, Electrochim. Acta, 52, 681.
36. Garcia-Vergara, S. J., Skeldon, P., Thompson, G. E., Hashimoto, T. and Habazaki, H. 2007, J. Electrochem. Soc., 154, C540.
37. Houser, J. E. and Hebert, K. R. 2009, Nat. Mater., 8, 415.
38. Çapraz, Ö. Ö., Shrotriya, P., Skeldon, P., Thompson, G. E. and Hebert, K. R. 2015, Electrochim. Acta, 159, 16.
39. Çapraz, Ö. Ö., Shrotriya, P., Skeldon, P., Thompson, G. E. and Hebert, K. R. 2015, Electrochim. Acta, 167, 404.
40. Mirzoev, R. A., Davydov, A. D., Zarubenko, E. S., Vystupov, S. I. and Panteleev, E. S. 2016, Electrochim. Acta, 218, 74.
41. Mirzoev, R. A., Davydov, A. D., Vystupov, S. I., Zarubenko, E. S., Kabanova, T. B. and Popkovich, A. V. 2017, Electrochim. Acta, 243, 270.
42. Zhu, X. F., Li, D. D., Song, Y. and Xiao, Y. H. 2005, Mater. Lett., 59, 3160.
43. Zhu, X., Liu, L., Song, Y., Jia, H., Yu, H., Xiao, X. and Yang, X. 2008, Mater. Lett., 62, 4038.
44. Zhu, X., Liu, L., Song, Y., Jia, H., Yu, H., Xiao, X. and Yang, X. 2008, Monatsh. Chem., 139(9), 999.
45. Yang, X., Zhu, X., Jia, H. and Han, T. 2009, Monatsh. Chem., 140, 595.
46. Ruiquan, Y., Longfei, J., Xufei, Z., Ye, S., Dongliang, Y. and Aijun, H. 2012, RSC Adv., 2(32), 12474.
47. Zhu, X., Song, Y., Yu, D., Zhang, C. and Yao, W. 2013, Electrochem. Commun., 29, 71.
48. Li, D., Jiang, C., Jiang, J. and Lu, J. G. 2009, Chem. Mater., 21(2), 253.
49. Li, D., Zhao, L., Jiang, C. and Lu, J. G. 2010, Nano Lett., 10(8), 2766.
50. Zaraska, L., Jaskuła, M. and Sulka, G. D. 2016, Mater. Lett., 171, 315.
51. Patermarakis, G. and Triantis, T. M. 2019, Curr. Top. Electrochem., 21, 21.
52. Belca, I., Kasalica, B., Zekovic, L., Jovanic, B. and Vasilic, R. 1999, Electrochim. Acta, 45(6), 993.
53. Patermarakis, G. and Kapiris, G. 2013, J. Solid State Electrochem., 17(4), 1133.
54. Patermarakis, G. and Plytas, J. 2016, J. Electroanal. Chem., 769, 97.
55. Patermarakis, G. 2014, J. Electroanal. Chem., 730, 69.
56. Mirzoev, R. A., Davydov, A. D., Vystupov, S. I. and Kabanova, T. B. 2019, Electrochim. Acta, 294, 276.
57. Atkins, P. 2010, Physical Chemistry, Oxford University Press.
58. Weast, R. C. (Ed.), 1980, Handbook of Chemistry and Physics, Sixtieth Ed., CRC Press, Boca Raton, pp. B-82, B-104, D-67, F-43, F-214, F-245.
59. Patermarakis, G., Lenas, P., Karavassilis, C. and Papayiannis, G. 1991, Electrochim. Acta, 36(3-4), 709.
60. Patermarakis, G., Chandrinos, J. and Masavetas, K. 2007, J. Solid State Electrochem., 11, 1191.
61. Filatova, E. O., Konashuk, A. S. 2015, J. Phys. Chem. C, 119(35), 20755-20761.
62. Albella, J. M., Montero, I. and Martinez-Duart, J. M. 1987, Electrochim. Acta, 32, 255.
63. Crossland, A. C., Habazaki, H., Shimizu, K., Skeldon, P., Thompson, G. E., Wood, G. C., Zhou, X. and Smith, C. J. E. 1999, Corros. Sci., 41, 1945.
64. Thompson, G. E., Furneaux, R. C. and Wood, G. C. 1978, Corros. Sci., 18, 481.
65. Purcell, E. M. 1965, Electricity and Magnetism, Berkeley Physics Course Vol. II, Education Development Center.
66. Marcus, Y. 1988, Chem. Rev., 88, 1475.
67. Ebbing, D. D. and Gammon, S. D. 2013, General Chemistry, Tenth Intl. Ed., Cengage Learning, Boston USA.

68. Brown, T. L., LeMay, H. E., Bursten, B. E., Murphy, C. J., Woodward, P. M. and Stoltzfus, M. W. 2018, Chemistry: The Central Science, Thirteenth Ed., Pearson Education, USA.
69. Patermarakis, G. and Fountoukidis, E. 1990, Water Res., 24, 1491.
70. Patermarakis, G., Moussoutzanis, K. and Chandrinos, J. 2001, J. Solid State Electrochem., 6, 39.
71. Rossmeisl, J., Qu, Z.-W., Zhu, H., Kroes, G.-J. and Nørskov, J. K. 2007, J. Electroanal. Chem. 607, 83-89.
72. Dobos, D. 1975, Electrochemical Data: A Handbook for Electrochemists in Industry and Universities, Elsevier.
73. Davies, C. W. 1967, Electrochemistry, Newness, London.
74. Gerasimov, Ya., Ed., Dreving, V., Eremin, E., Kiselev, A., Lebedev, V., Panchenkov, G. and Shlygin, A. 1974, Physical Chemistry, Mir Publishers, Moscow.
75. Georgiou, D., Kalis, M., Patermarakis, G. and Vassiliadis, A. 2017, Curr. Trends Fashion Technol. Textile Eng., 1(2), CTFTTE.MS.ID.555560.
76. Patermarakis, G. and Moussoutzanis, K. 2002, J. Solid State Electrochem., 6(7), 475.
77. Vogel, A. I. 1976, Macro and Semimicro Quantitative Analysis, Longman, London.
78. Alexeyev, V. N. 1980, Qualitative Chemical Analysis, Mir Publishers, Moscow.
79. Zaraska, L., Brudzisz, A., Wierzbicka, E. and Sulka, G. D. 2016, Electrochim. Acta, 198, 259.